

pubs.acs.org/cm Article

Phase-Controllable Synthesis of Ultrathin Molybdenum Nitride Crystals Via Atomic Substitution of MoS₂

Hongze Gao, Jun Cao, Tianshu Li, Weijun Luo, Mason Gray, Narendra Kumar, Kenneth S. Burch, and Xi Ling*



Cite This: https://doi.org/10.1021/acs.chemmater.1c03712



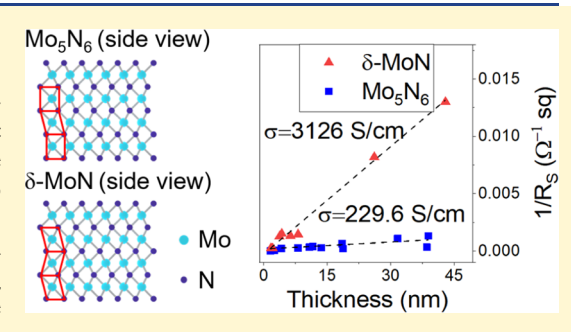
ACCESS I

Metrics & More

Article Recommendations

s Supporting Information

ABSTRACT: MXenes are emerging members in the two-dimensional (2D) material family and are highlighted by their high electrical conductivity. Among different MXenes, molybdenum-based MXenes, especially molybdenum nitrides (MoN_x), are rarely accessible through the common synthetic approach of selective etching due to the absence of stable MAX phase precursors. In this work, we apply the atomic substitution approach to synthesize two phases of ultrathin nonlayered molybdenum nitrides (i.e., Mo₅N₆ and δ-MoN) from 1.6 to 42.9 nm thickness by converting layered MoS₂ under different temperatures. The morphology and 2D nature of MoS₂ are well remained in both phases. These newly created 2D materials are further characterized using Raman spectroscopy, high-resolution transmission



electron microscopy, and electrical measurements, suggesting that both phases are highly crystalline and highly conductive down to the thickness of a few nanometers. Moreover, Ohmic contacts are formed between the ultrathin nitrides and Cr/Au electrodes, suggesting the great potential of the obtained nitrides for nanoelectronic device applications. The stability test shows that the Ohmic contact is well maintained after 4 weeks under ambient conditions with a slight degradation in conductivity. This study extends the 2D family by providing highly conductive members, offering desired building blocks for solid-state nanoelectronic devices.

■ INTRODUCTION

Since the first successful synthesis of two-dimensional (2D) titanium carbide $(Ti_3C_2T_x)$ in 2011, a new group of 2D materials, MXenes (i.e., 2D transition-metal carbides, carbonitrides, and nitrides), have been introduced into the 2D family. MXenes have drawn tremendous interest among researchers by virtue of their excellent electrical, optical, and mechanical properties,²⁻⁴ with potential in various applications including energy storage, transparent conductors, and gas sensors.⁵⁻¹ Among a variety of synthetic strategies, selective etching of bulk MAX phase precursors is the most widely used one to make MXenes. 9-11 Nevertheless, molybdenum-based MXenes, especially molybdenum nitrides (MoN_x), are hardly accessible through this approach due to the rarity of stable MAX precursors from theoretical predictions. 12,13 Thus, alternative synthetic strategies beyond the selective etching method are in demand. Growing efforts have been spent on designing rational synthetic routes for 2D molybdenum-based MXenes very recently. 14-24 Synthesis of 2D Mo₂C has been achieved through a chemical vapor deposition (CVD) process.²¹⁻²³ With regard to MoN_x, Hong et al. developed an approach to grow monolayer MoSi₂N₄ by introducing silicon during the deposition of Mo₂N film using the CVD technique.¹⁴ The presence of silicon atoms passivates the surface and hence enables the lateral growth of the film. A single-crystal flake of up to 20 μ m can be obtained using this method. P-type

semiconducting behavior and a high Young's modulus of 491.4 GPa were observed for the as-prepared $MoSi_2N_4$ film, suggesting its great electrical and mechanical properties. In addition, the synthesis of 2D Mo_5N_6 with tunable thickness down to a few nanometers has been achieved by Cao et al. via a selective atomic substitution method, where 2D MoS_2 flakes are used as precursors to react with ammonia to obtain ultrathin Mo_5N_6 . The product flake has a low sheet resistance comparable to CVD graphene. These methods offer access to highly crystalline and tens-of-micrometer-sized metal nitrides, especially molybdenum nitrides, building the foundation for future exploration of their physics and applications in electronic devices.

A variety of MoN_x with different stoichiometries and crystal structures have been reported in either bulk or 2D forms, including MoN₂, Mo₅N₆, δ -MoN, β -Mo₂N, and γ -Mo₂N. ^{15–19,25–27} All MoN_x are composed of host Mo atoms and interstitial N atoms. Three of the polymorphisms (MoN₂, Mo₅N₆, and δ -MoN) belong to the hexagonal crystal system,

Received: October 26, 2021 Revised: December 11, 2021



while β -Mo₂N belongs to the tetragonal crystal system, and γ -Mo₂N belongs to the cubic crystal system. With the density of states around the Fermi level being significantly modified by the interstitial N atoms, the concentration of nitrogen has a remarkable impact on the electrical properties of MoN_x (e.g., electrical conductivity).²⁵ Nonetheless, reports on achieving the different phases of ultrathin MoN_x, especially those with satisfactory lateral dimensions for electronic devices, are very rare. 16,17 Guy et al. synthesized different phases of nanostructured Mo₂N and Mo₅N₆ in a powder form by using metalorganic clusters as precursors, 17 and Jin et al. reported that the addition of foreign elements in nitrogen-deficient δ -MoN nanosheets could result in the formation of nitrogen-rich Mo₅N₆ nanosheets. 16 Note that these works are not focusing on the lateral size of the materials (mostly below 500 nm), and hence the as-synthesized materials do not meet the requirements for solid-state electronic devices. Thus, it is important to study whether different phases of ultrathin MoN_x with high crystallinity and relatively large lateral size (\sim 10 μ m) can be synthesized for the studies in fundamental physics and device applications.

Building on our recent development of atomic substitution strategy for ultrathin metal nitrides that are suitable for electronic devices, 15 hereby we further apply this strategy to the synthesis of different phases of MoN_x (i.e., Mo_5N_6 and δ -MoN). We demonstrate that two different phases of highly crystalline ultrathin MoN_x can be acquired using the atomic substitution approach, and the morphologies of the materials inherit from the MoS₂ precursors. Benefiting from the easy tuning of the MoS₂ thickness, MoN_r flakes of a variety of thicknesses are obtained. We further investigate the electrical properties of both phases down to a few nanometers, and high electrical conductivities (i.e., 229.6 S cm⁻¹ for Mo₅N₆ and 3126 S cm $^{-1}$ for δ -MoN) with excellent stability under ambient conditions are observed. The new 2D members obtained in this work extend the 2D family and provide promising electrode materials that could serve as building blocks for future 2D material-based electronic devices.

MATERIALS AND METHODS

Conversion for Different Phases of MoN_x. MoS₂ flakes of different thicknesses were mechanically exfoliated from a single crystalline bulk crystal using Scotch tape and then transferred onto a SiO₂/Si substrate with a SiO₂ layer of 300 nm thickness. The substrates were cleaned by sonication in acetone, isopropyl alcohol, and deionized water in sequence, 10 min for each step, followed by O₂ plasma cleaning. The conversion was conducted in a quartz tube with argon (50 sccm) as the carrier gas, heated by a tube furnace. A crucible filled with urea (500 mg) was placed at the lower temperature zone at the upper stream to generate ammonia through the decomposition reaction of urea, and the SiO₂/Si chip with MoS₂ flakes on it was held by another crucible in the middle of the heating zone. The temperature was set to ramp from room temperature to the target temperature (650-1000 °C) under the rate of 30 °C/min, followed by maintaining at the target temperature for 10 h to ensure a complete phase transition between MoN_x. Afterward, the furnace was cooled to room temperature naturally.

Material Characterizations. The as-prepared MoN_x was characterized using Raman spectroscopy, atomic force microscopy (AFM), and high-resolution transmission electron microscopy (HRTEM). Raman and photoluminescence (PL) measurements were performed on a Renishaw inVia Raman microscope equipped with a 532 nm laser line. All spectra were taken using the same condition with a laser power of 0.27 mW. AFM topography was acquired using a Bruker dimension system. TEM measurements were

performed using an FEI Tecnai Osiris transmission electron microscope operating at a 200 kV accelerating voltage.

Electrode Fabrication and Electrical Measurements. All electrodes were fabricated inside a cleanroom in a glovebox. The electrode patterning was done using a bilayer photoresist (LOR1A/S1805) and laser mask writer (Heidelberg Instruments). Then, Au/Cr (30 nm/20 nm) was deposited using e-beam evaporation followed by lift-off using remover PG (MicroChem).

In the transfer length method (TLM), the relationship between total resistance ($R_{\rm total}$), contact resistance ($R_{\rm contacts}$), and channel resistance ($R_{\rm channel}$) can be described by the following equation:

$$R_{\text{total}} = R_{\text{channel}} + R_{\text{contacts}} = R_{\text{s}} \frac{1}{W} + R_{\text{contacts}}$$

In the equation above, $R_{\rm s}$ is the sheet resistance of the sample, l is the length of the channel, and w is the width of the channel. For a flake with uniform thickness, the $R_{\rm total}$ versus $\frac{l}{w}$ curve can be fitted with a linear function, whose slope is $R_{\rm s}$ and Y-intercept is $R_{\rm contacts}$.

To find out electrical conductivity (σ) from R_{s} , a plot of $\frac{1}{R_{s}}$ versus h

is shown in Figure 4d. The conductivity can be extracted by expanding the expression of sheet resistance through the following equation:

$$\rho = \frac{1}{\sigma} = R_s \cdot h$$

$$\frac{1}{R_s} = \sigma \cdot h$$

with ρ being the electrical resistivity and h being the thickness of the sample. Therefore, by fitting the $\frac{1}{R_s}$ versus h curve into a linear function, the value of σ can be found from the slope of the fitting line. In Figure 5, R_s is plotted as a function of h in the log scale. The

relationship can be described as:
$$\log_{10} R_{\rm s} = \log_{10} \rho - \log_{10} h$$

$$\log_{10} \frac{1}{R_s} = \log_{10} \sigma + \log_{10} h$$

Hence, the *Y*-intercept of each fitting line is the conductivity of the material in the logarithm scale.

RESULTS

The crystal structures of the two phases of MoN_x (i.e., Mo₅N₆ and δ -MoN) are shown in Figure 1a. The spatial distributions of Mo atoms in both crystals follow the hexagonal honeycomb structure in the basal plane with AA stacking of Mo atoms out of the basal plane. N atoms are located at the interstitial sites of Mo atoms with different arrangements out of the basal plane (AABB for Mo₅N₆ and ABAB for δ -MoN).²⁶ In addition, different from the vacancy-free δ -MoN crystals, there are randomly distributed Mo vacancies in the Mo₅N₆ lattice, resulting in a different stoichiometry. To obtain MoN, we apply a nitridation reaction on MoS2 by introducing ammonia to a horizontal quartz tube furnace heated at ~700 °C, in which MoS₂ flakes on a SiO₂/Si substrate are placed at the center of the heating zone (see Figure S1 for the setup). By controlling the reaction temperature, we find that both Mo₅N₆ and δ -MoN can be obtained (detailed characterizations using HRTEM are discussed later). Figure 1b summarizes the temperature condition for each phase. When the reaction temperature falls in between 650 and 685 °C, Mo₅N₆ is obtained as the product, while δ -MoN will be obtained when the reaction temperature is between 685 and 1000 °C. The conversion is barely observed below 650 °C, and cracks appear

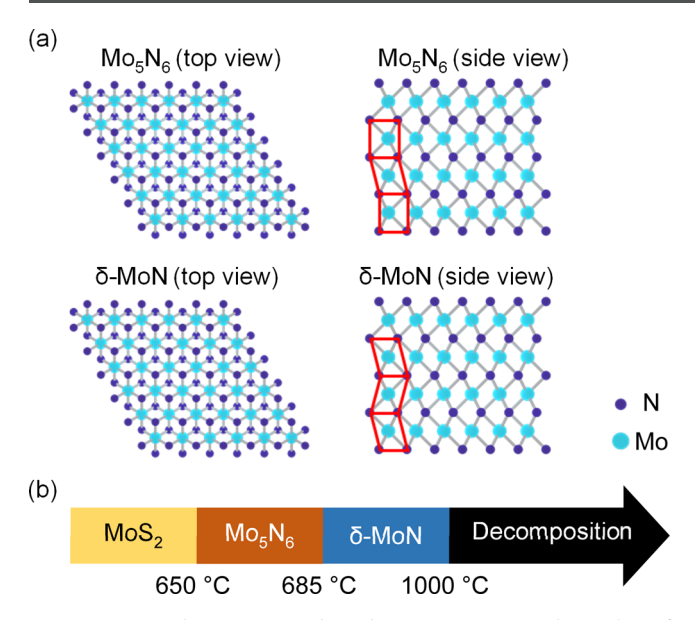


Figure 1. Crystal structures and product—temperature relationship of the reaction. (a) Crystal structures of Mo_5N_6 and δ-MoN. The arrangements of nitrogen atoms in Mo_5N_6 (AABB) and δ-MoN (ABAB) out of the basal plane are labeled by red lines. (b) Products of the reaction at different temperatures. Below 650 °C: no new product. 650–685 °C: Mo_5N_6 . 685–1000 °C: δ-MoN. Above 1000 °C: decomposition.

on the flakes at the high-temperature limit of >1000 °C (Figure S2), suggesting the decomposition of MoN_x . The temperature for the in situ phase transition is close to the reported value for MoN_x nanosheets. Note that the other member of hexagonal MoN_x (i.e., MoN_2) is unstable above 550 °C under atmospheric pressure. Since this temperature is even lower than the temperature where the nitridation reaction is enabled, MoN_2 has not been obtained as a product of the conversion.

Apart from the reaction temperature, the duration also plays an important role in the phase transition. In our previous work, we reported the synthesis of Mo_5N_6 through such a substitutional reaction at 850 °C for 1 h¹⁵ Although the

requirement for phase transition from Mo_5N_6 to δ -MoN has been fulfilled thermodynamically under this condition, the transition rate could be low enough that a little portion of Mo_5N_6 is converted into δ -MoN. As a result, the majority of the sample retained as Mo_5N_6 . In this work, the reaction time is significantly extended (from 1 to 10 h) to make sure thermal equilibrium has been established in the phase transition process, and thus, the final product is mainly controlled by the temperature.

Figure 2 shows the optical and AFM images of flakes before and after conversion. Two MoS₂ flakes around 9 nm thick are shown as examples to demonstrate the typical change in optical images and thicknesses. A substantial change in optical contrast is observed after MoS₂ flakes are converted into either Mo₅N₆ or δ -MoN, where the pale-yellow color of MoS₂ turns into dark blue. This change in optical contrast results from the significantly modified absorption spectra due to the distinct electronic band structures. ¹⁵ Nevertheless, the shapes and smooth surfaces of the flakes are well maintained throughout the conversion, which is observed from both optical images (Figure 2a-d) and AFM images (insets of Figure 2a-d). The height profiles extracted from the AFM images of the flakes are shown in Figure 2e and f, presenting a drastic reduction in thickness through the conversion, where the thickness decreases from 9.3 to 4.9 nm (corresponds to a reduction to 52.6% of the original thickness of MoS₂) for the conversion from MoS₂ to Mo₅N₆ and from 9.6 to 5.3 nm (corresponds to a reduction to 56.2% of the original thickness of MoS₂) for δ -MoN. With the Van der Waals gap in MoS2 replaced by Mo-N bonds in MoN_x , the distance between two adjacent layers of Mo atoms in MoN_x is expected to reduce to 37.2% (Mo₅N₆) and 37.7% (δ -MoN) of the original distance in MoS₂. Considering the existence of gaps between the flakes and substrates, our experimental results match with the theoretical values. By using MoS₂ flakes of various thicknesses, we further obtain MoN, flakes of different thicknesses ranging from a few nanometers to tens of nanometers (for AFM images, see Figure S3 of the Supporting Information).

To distinguish and identify the two different phases of MoN_x , we performed Raman spectroscopy and HRTEM characterizations on the converted flakes. Raman spectra of

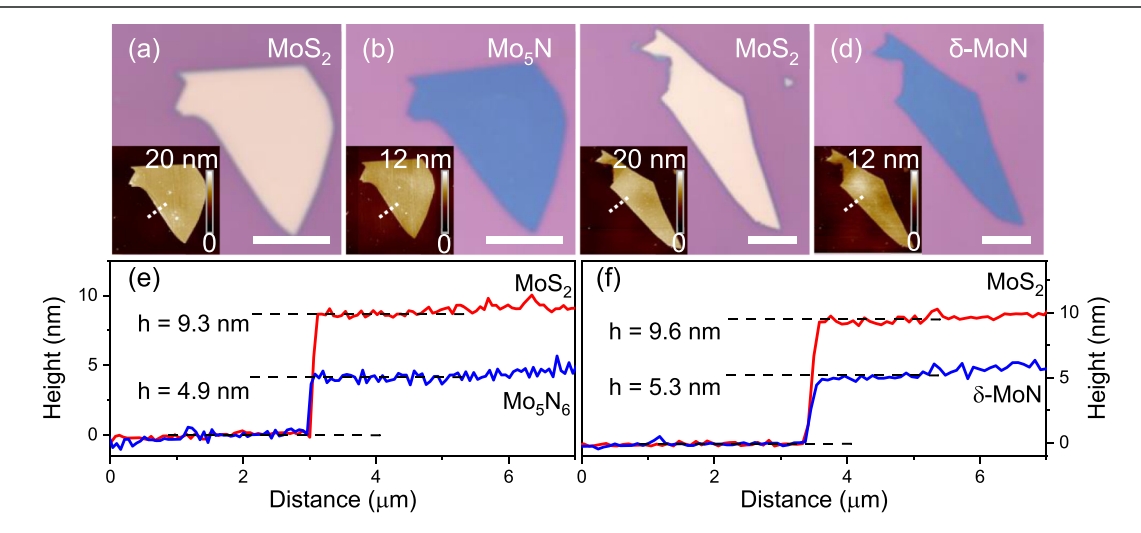


Figure 2. Optical and AFM images of MoS₂, Mo₅N₆, and δ-MoN flakes. (a–d) Optical microscope images of MoS₂ (a, c), Mo₅N₆ (b), and δ-MoN (d) flakes. All scale bars: 5 μ m. Insets: AFM image of the corresponding flake. (e,f) Height profiles of Mo₅N₆ (e) and δ-MoN (f) flakes before and after conversion, measured along the white dash lines in the AFM images.

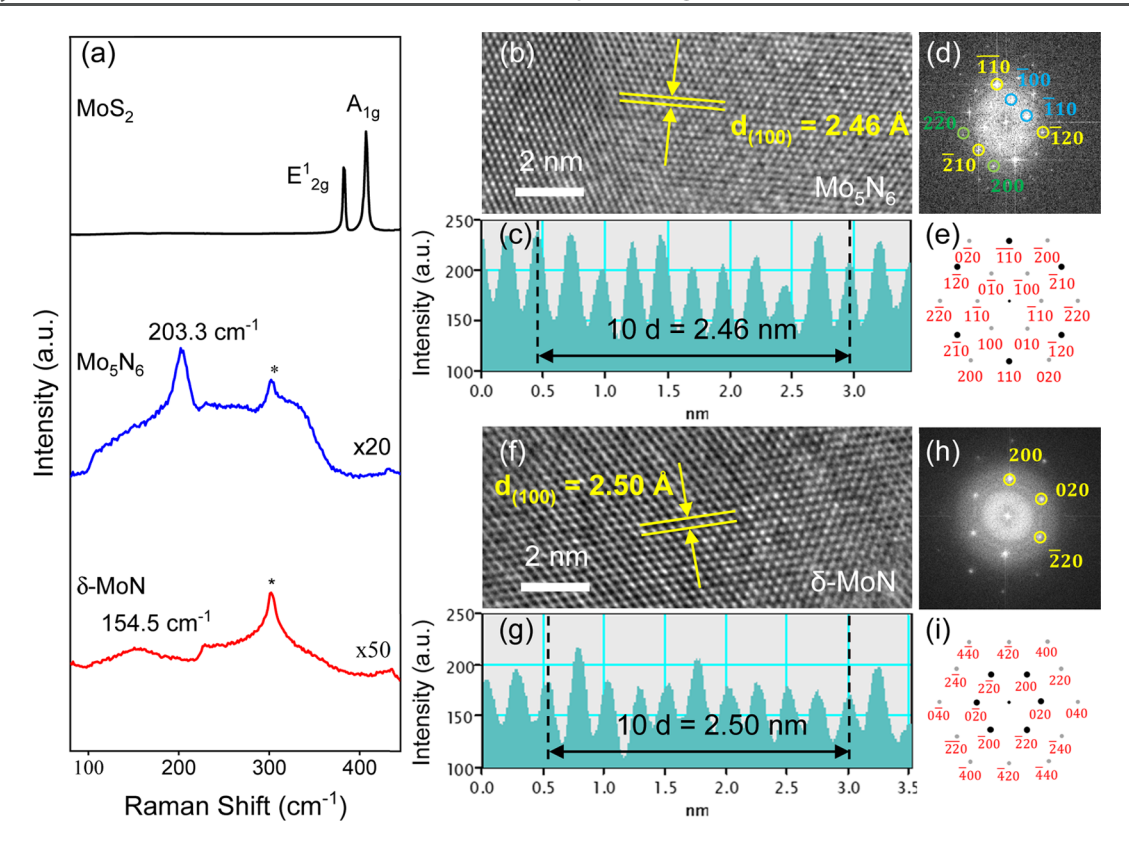


Figure 3. Raman spectroscopy and TEM characterization of MoN_{x^*} (a) Raman spectra of MoS_2 , Mo_3N_6 , and δ-MoN. Peaks from the substrates are labeled with *. (b, f) HRTEM images of Mo_3N_6 (b) and δ-MoN (f). The interplanar distances are measured between the planes labeled by the solid white lines. (c, g) Intensity profiles of Mo_3N_6 (c) and δ-MoN (g) extracted from the corresponding HRTEM image. (d, h) FFT patterns converted from the HRTEM images of Mo_3N_6 (d) and δ-MoN (h). (e, i) Simulated selected area electron diffraction patterns of Mo_5N_6 (e) and δ-MoN (i) crystals.

 MoS_2 and MoN_x are shown in Figure 3a. The two strongest peaks of MoS_2 , the E^1_{2g} and A_{1g} modes,³¹ vanish after the conversion, and a new peak around 210 cm⁻¹ appears for Mo_5N_6 and a broad peak centered at 150 cm⁻¹ appears for δ -MoN. The distinct Raman spectra of MoN_x offer a fast and convenient approach for the distinguishment of different phases. Moreover, the PL peaks of MoS₂ disappear after conversion with no new peaks observed (Figure S4), which is expected, given that the band structures of both MoN_x are significantly different from that of MoS₂. A detailed structural characterization using HRTEM was performed to identify the two phases of MoN_x. As shown in Figure 3b and f, the lattice plane distance is extracted to be 2.46 and 2.50 Å, matching well with the interplanar distance of (100) plane of Mo₅N₆ (2.45 Å) and (100) plane of δ -MoN (2.48 Å), ²⁶ respectively. The intensity profiles across the lattice planes are shown in Figure 3c and g. Apart from the interplanar distance, fast Fourier transformation (FFT) patterns further confirm the two phases. As shown in Figure 3d, the FFT pattern of Mo_5N_6 showed a set of primary peaks distributed in a hexagon (labeled by yellow circles) and two sets of secondary hexagonal peaks around the primary peaks (labeled by green and blue circles). Different from Mo₅N₆, the FFT pattern of δ -MoN (Figure 3h) shows only one set of primary peaks with no secondary peaks. These results match well with the simulated diffraction patterns of Mo_5N_6 and δ -MoN crystals (Figure 3e and i), respectively.

As a highly conductive member in the 2D family, we further performed the electrical conductivity measurements to

evaluate the potential of these ultrathin MoN_x in nanoelectronic devices. We fabricated 20 MoN_x samples with Cr/ Au electrodes using the cleanroom in a glovebox system²⁸ and performed electrical measurements on the samples. TLM was used to extract the sheet resistance of the samples while eliminating the influence of contact resistance. As shown in the schematic illustration in Figure 4a, multiple electrodes with designed physical separations are deposited onto the samples for various channel lengths, where the channel lengths range from 1.25 to 13.54 μ m. Details about the TLM can be found in the experimental section. Figure 4b and c shows the optical image and I-V curves from channels with different lengths of a 2.1 nm thick δ -MoN flake. The linear trend of the I-V curve indicates an Ohmic contact between δ -MoN and the Cr/Au electrode. The total resistance of each channel is plotted as a function of the aspect ratio $(\frac{1}{n})$, where l and w are the length and width of the channel, respectively) of the channel in the inset of Figure 4c and then fitted into a linear function to find out R_s . Considering that R_s is an extrinsic property that depends on the thickness of the sample, we obtained the R_s of Mo_5N_6 and δ -MoN with different thicknesses ranging from 1.6 to 42.9 nm. Then, $\frac{1}{R_c}$ as a function of h is plotted in Figure 4d with a linear fitting applied to the data to obtain the electrical conductivity, which is a property that does not depend on the thickness of the samples. All data points are listed in Table S1. We find that the σ of Mo₅N₆ (229.6 S cm⁻¹) is approximately 1 order lower than that of δ -MoN (3126 S cm⁻¹), where negligible thickness dependence is observed in σ for both

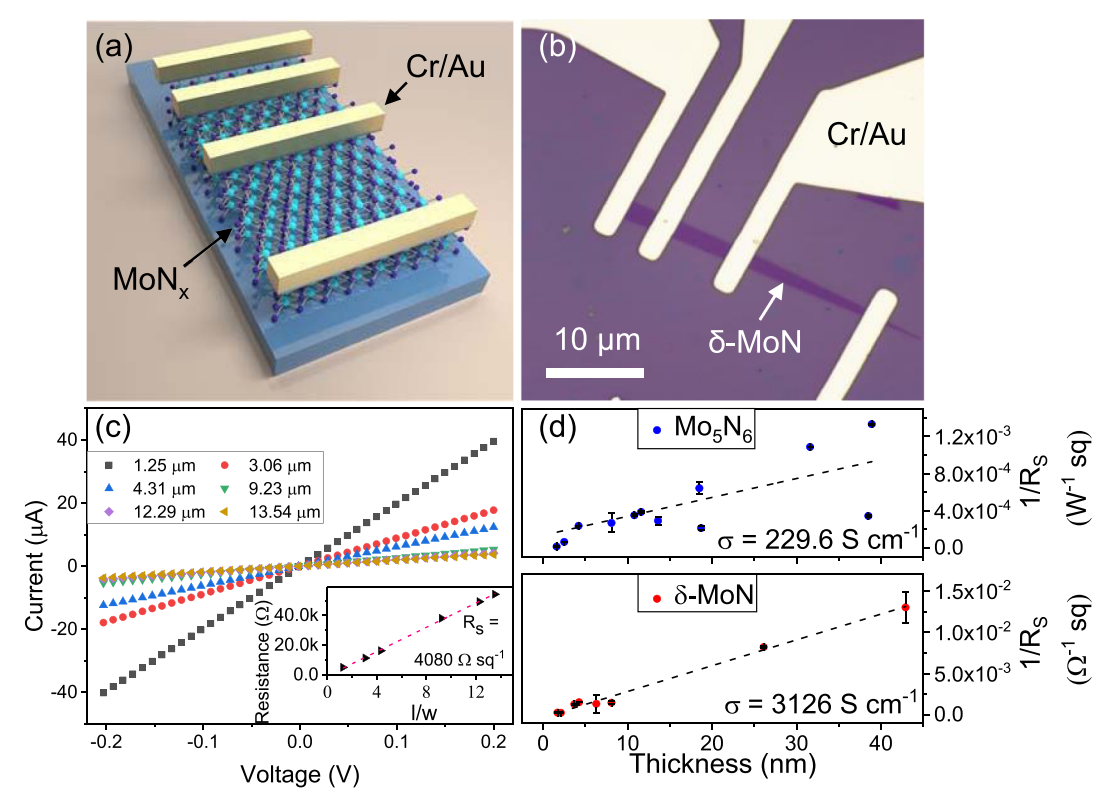


Figure 4. Electrical characterization of Mo_5N_6 and δ-MoN. (a) Schematic illustration of the TLM. (b) Typical optical image of electrodes fabricated on a 2.1 nm thick δ-MoN flake. (c) I-V curve of the sample shown in (b). Inset: R-I/W curve fitted into a linear function. (d) Plot of I/R_8 versus thickness for Mo_5N_6 (bottom) and δ-MoN (top) with linear fitting lines. Error bars present the standard error of each data point.

 MoN_x . Although it has not yet been verified by experimental results, we hypothesize that the lower conductivity of Mo_5N_6 can be attributed to the presence of randomly distributed Mo vacancies throughout the crystal. Based on the XPS results in our previous work, ¹⁵ the oxidation state in Mo_5N_6 is dominated by the +4 state, in which case the formation of Mo vacancies can be described by the following equation:

$$4e^{-} + Mo_{Mo} = V_{Mo}^{-4} + Mo$$

where e^- stands for free electrons in the crystal, Mo_{Mo} stands for Mo atoms located on their lattice sites, V_{Mo}^{-4} stands for the negatively charged Mo vacancies, and Mo stands for the Mo atoms leaving the crystal during the reaction. Upon generation of one Mo vacancy, four free electrons will be vanished to balance the negative effective charge of this vacancy to obey the law of charge conservation. This leads to the decrement of free electron concentration throughout the crystal, thus lowering the electrical conductivity of Mo_5N_6 compared to the vacancy-free $\delta\text{-MoN}$ samples.

We further compared the electrical conductivities of MoN_x with other widely studied metallic 2D materials, including CVD graphene, 32 Ti $_3C_2T_x$, $^{2,33-35}$ and 1T-MoS $_2$, 36,37 with results shown in Figure 5. Comparison with more emerging metallic 2D materials is presented in Table S2. $^{38-41}$ In Figure 5, the sheet resistances of each material at different thicknesses are plotted and fitted into linear functions (details in the experimental section). The *Y*-intercept of each fitting line on the right *Y*-axis stands for the electrical conductivity of the corresponding material. From Figure 5, we found that the electrical conductivity of δ -MoN (3126 S cm $^{-1}$) is fairly high and comparable to Ti $_3C_2T_x$ (3092–6450 S cm $^{-1}$), which is one of the most extensively studied MXenes in recent years. 12

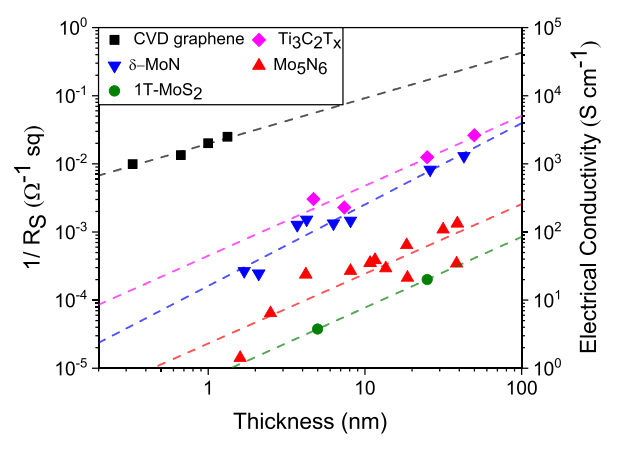


Figure 5. Comparison of the electrical conductivity among Mo_5N_6 , δ -MoN, CVD graphene, 32 $Ti_3C_2T_{\omega}^{-2,33-35}$ and 1T-MoS $_2$. 36,37 Data are plotted in the log scale with linear fitting functions.

Considering the self-aligned MoS₂–MoN_x lateral heterostructure observed in our previous work, MoN_x shows great potential as contact electrode materials for MoS₂-based electronic devices. Compared with 1T-MoS₂, which also forms a self-aligned heterostructure with ultrathin 2H–MoS₂ resulting in a low-resistance Ohmic contact, both MoN_x have noticeably higher electrical conductivities, suggesting the promising potential of MoN_x as electrode materials in nanodevices.

Importantly, apart from the high electrical conductivities, MoN_x also shows excellent stability under ambient conditions, which is a missing property in most MXenes and $1T-MoS_2$. ^{43,44} To demonstrate the stability of MoN_x , we recurringly

measured the electrical conductivity of eight samples (four from each phase) of different thicknesses every week for 4 weeks, while the samples are kept under ambient conditions. Results are shown in Figures S5–S7. The linear shape of I-V curves was well maintained throughout the whole period, while the electrical conductivity dropped to $73.36 \pm 4.31\%$ (Mo_5N_6) and $75.61 \pm 4.49\%$ (δ -MoN) of the original values. As a comparison, the electrical conductivity of $Ti_3C_2T_x$ decreased by approximately 1 order of magnitude under the same conditions. The results demonstrate the excellent electrical stability of our ultrathin MoN_{xy} offering promising highly conductive materials for 2D material-based devices.

CONCLUSIONS

In this work, we demonstrate that two different phases of highly crystalline ultrathin molybdenum nitrides, that is, Mo_5N_6 and δ -MoN, can be obtained through a phase controllable atomic substitution reaction of MoS2 at different temperatures. The resultant MoN_x flakes inherit the morphology and smooth surface from MoS2 flakes. Both MoNx have characteristic Raman spectra for fast distinguishment. Electrical measurements reveal the formation of Ohmic contacts between MoN_x and Cr/Au electrodes. High electrical conductivities of Mo_5N_6 (229.6 S cm⁻¹) and δ -MoN (3126 S cm⁻¹) down to a few nanometers are extracted via TLM. The stability test shows that MoN_x samples maintain high conductivity with minor degradation under ambient conditions after 4 weeks. Our work introduces two highly conductive members with outstanding stability to the 2D material family, offering desirable electrode materials for future solid-state nanoelectronic devices.

ASSOCIATED CONTENT

Supporting Information

The Supporting Information is available free of charge at https://pubs.acs.org/doi/10.1021/acs.chemmater.1c03712.

Additional optical and AFM images, supporting PL spectra, all conductivity data for 20 samples, comparison of MoN_x and other metallic 2D materials, and data of stability tests (PDF)

AUTHOR INFORMATION

Corresponding Author

Xi Ling — Department of Chemistry, Boston University, Boston, Massachusetts 02215, United States; Division of Materials Science and Engineering, Boston University, Boston, Massachusetts 02215, United States; orcid.org/0000-0003-3462-9088; Email: xiling@bu.edu

Authors

Hongze Gao – Department of Chemistry, Boston University, Boston, Massachusetts 02215, United States

Jun Cao – Department of Chemistry, Boston University, Boston, Massachusetts 02215, United States

Tianshu Li — Division of Materials Science and Engineering, Boston University, Boston, Massachusetts 02215, United States

Weijun Luo – Department of Chemistry, Boston University, Boston, Massachusetts 02215, United States

Mason Gray − Department of Physics, Boston College, Boston, Massachusetts 02467, United States; ocid.org/0000-0002-2778-9166

Narendra Kumar – Department of Physics, Boston College, Boston, Massachusetts 02467, United States; orcid.org/ 0000-0002-5319-1547

Kenneth S. Burch – Department of Physics, Boston College, Boston, Massachusetts 02467, United States; orcid.org/ 0000-0002-7541-0245

Complete contact information is available at: https://pubs.acs.org/10.1021/acs.chemmater.1c03712

Notes

The authors declare no competing financial interest.

ACKNOWLEDGMENTS

Work at the Boston University was supported by the U.S. Department of Energy (DOE), Office of Science, Basic Energy Sciences (BES) under award DE-SC0021064. X.L. acknowledges the membership of the Photonics Center at the Boston University. Work done by M.G. is supported by the National Science Foundation DMR-2003343. N.K. is grateful to the support provided by the Office of Naval Research under award number N00014-20-1-2308. Work by K.S.B. was done with support from the Department of Energy (DOE), Office of Science, Office of Basic Energy Sciences under Award No. desc0018675.

REFERENCES

- (1) Naguib, M.; Kurtoglu, M.; Presser, V.; Lu, J.; Niu, J.; Heon, M.; Hultman, L.; Gogotsi, Y.; Barsoum, M. W. Two-Dimensional Nanocrystals Produced by Exfoliation of Ti₃AlC₂. *Adv. Mater.* **2011**, 23, 4248–4253.
- (2) Dillon, A. D.; Ghidiu, M. J.; Krick, A. L.; Griggs, J.; May, S. J.; Gogotsi, Y.; Barsoum, M. W.; Fafarman, A. T. Highly Conductive Optical Quality Solution-Processed Films of 2D Titanium Carbide. *Adv. Funct. Mater.* **2016**, 26, 4162–4168.
- (3) Hart, J. L.; Hantanasirisakul, K.; Lang, A. C.; Anasori, B.; Pinto, D.; Pivak, Y.; van Omme, J. T.; May, S. J.; Gogotsi, Y.; Taheri, M. L. Control of MXenes' Electronic Properties through Termination and Intercalation. *Nat. Commun.* **2019**, *10*, 522.
- (4) Naguib, M.; Mochalin, V. N.; Barsoum, M. W.; Gogotsi, Y. 25th Anniversary Article: MXenes: A New Family of Two-Dimensional Materials. *Adv. Mater.* **2014**, *26*, 992–1005.
- (5) Peng, Y.-Y.; Akuzum, B.; Kurra, N.; Zhao, M.-Q.; Alhabeb, M.; Anasori, B.; Kumbur, E. C.; Alshareef, H. N.; Ger, M.-D.; Gogotsi, Y. All-MXene (2D Titanium Carbide) Solid-State Microsupercapacitors for on-Chip Energy Storage. *Energy Environ. Sci.* **2016**, *9*, 2847–2854.
- (6) Hantanasirisakul, K.; Zhao, M.-Q.; Urbankowski, P.; Halim, J.; Anasori, B.; Kota, S.; Ren, C. E.; Barsoum, M. W.; Gogotsi, Y. Fabrication of $\mathrm{Ti}_3\mathrm{C}_2\mathrm{T}_{\mathrm{x}}$ MXene Transparent Thin Films with Tunable Optoelectronic Properties. *Adv. Electron. Mater.* **2016**, *2*, 1600050.
- (7) Kim, S. J.; Koh, H.-J.; Ren, C. E.; Kwon, O.; Maleski, K.; Cho, S.-Y.; Anasori, B.; Kim, C.-K.; Choi, Y.-K.; Kim, J.; Gogotsi, Y.; Jung, H.-T. Metallic ${\rm Ti}_3{\rm C}_2{\rm T}_{\rm x}$ MXene Gas Sensors with Ultrahigh Signal-to-Noise Ratio. *ACS Nano* **2018**, *12*, 986–993.
- (8) Chertopalov, S.; Mochalin, V. N. Environment-Sensitive Photoresponse of Spontaneously Partially Oxidized Ti₃C₂ MXene Thin Films. ACS Nano 2018, 12, 6109–6116.
- (9) Alhabeb, M.; Maleski, K.; Anasori, B.; Lelyukh, P.; Clark, L.; Sin, S.; Gogotsi, Y. Guidelines for Synthesis and Processing of Two-Dimensional Titanium Carbide (${\rm Ti_3C_2T_x}$ MXene). *Chem. Mater.* **2017**, 29, 7633–7644.
- (10) Naguib, M.; Mashtalir, O.; Carle, J.; Presser, V.; Lu, J.; Hultman, L.; Gogotsi, Y.; Barsoum, M. W. Two-Dimensional Transition Metal Carbides. *ACS Nano* **2012**, *6*, 1322–1331.
- (11) Mashtalir, O.; Naguib, M.; Mochalin, V. N.; Dall'Agnese, Y.; Heon, M.; Barsoum, M. W.; Gogotsi, Y. Intercalation and

Delamination of Layered Carbides and Carbonitrides. *Nat. Commun.* **2013**, *4*, 1716.

- (12) Hantanasirisakul, K.; Gogotsi, Y. Electronic and Optical Properties of 2D Transition Metal Carbides and Nitrides (MXenes). *Adv. Mater.* **2018**, *30*, 1804779.
- (13) Frey, N. C.; Wang, J.; Vega Bellido, G. I.; Anasori, B.; Gogotsi, Y.; Shenoy, V. B. Prediction of Synthesis of 2D Metal Carbides and Nitrides (MXenes) and Their Precursors with Positive and Unlabeled Machine Learning. ACS Nano 2019, 13, 3031–3041.
- (14) Hong, Y.-L.; Liu, Z.; Wang, L.; Zhou, T.; Ma, W.; Xu, C.; Feng, S.; Chen, L.; Chen, M.-L.; Sun, D.-M.; Chen, X.-Q.; Cheng, H.-M.; Ren, W. Chemical Vapor Deposition of Layered Two-Dimensional MoSi₂N₄ Materials. *Science* **2020**, *369*, 670–674.
- (15) Cao, J.; Li, T.; Gao, H.; Lin, Y.; Wang, X.; Wang, H.; Palacios, T.; Ling, X. Realization of 2D Crystalline Metal Nitrides via Selective Atomic Substitution. *Sci. Adv.* **2020**, *6*, No. eaax8784.
- (16) Jin, H.; Liu, X.; Vasileff, A.; Jiao, Y.; Zhao, Y.; Zheng, Y.; Qiao, S.-Z. Single-Crystal Nitrogen-Rich Two-Dimensional Mo₅N₆ Nanosheets for Efficient and Stable Seawater Splitting. *ACS Nano* **2018**, *12*, 12761–12769.
- (17) Guy, K.; Tessier, F.; Kaper, H.; Grasset, F.; Dumait, N.; Demange, V.; Nishio, M.; Matsushita, Y.; Matsui, Y.; Takei, T.; Lechevalier, D.; Tardivat, C.; Uchikoshi, T.; Ohashi, N.; Cordier, S.; Guy, K. Original Synthesis of Molybdenum Nitrides Using Metal Cluster Compounds as Precursors: Applications in Heterogeneous Catalysis. Chem. Mater. 2020, 32, 6026–6034.
- (18) Wang, S.; Ge, H.; Sun, S.; Zhang, J.; Liu, F.; Wen, X.; Yu, X.; Wang, L.; Zhang, Y.; Xu, H.; Neuefeind, J. C.; Qin, Z.; Chen, C.; Jin, C.; Li, Y.; He, D.; Zhao, Y. A New Molybdenum Nitride Catalyst with Rhombohedral MoS₂ Structure for Hydrogenation Applications. *J. Am. Chem. Soc.* **2015**, *137*, 4815–4822.
- (19) Sun, G.-D.; Zhang, G.-H.; Chou, K.-C. Synthesis of Molybdenum Nitrides Nanosheets by Nitriding 2H-MoS₂ with Ammonia. *J. Am. Ceram. Soc.* **2018**, *101*, 2796–2808.
- (20) Guan, H.; Yi, W.; Li, T.; Li, Y.; Li, J.; Bai, H.; Xi, G. Low Temperature Synthesis of Plasmonic Molybdenum Nitride Nanosheets for Surface Enhanced Raman Scattering. *Nat. Commun.* **2020**, *11*, 3889.
- (21) Xu, C.; Wang, L.; Liu, Z.; Chen, L.; Guo, J.; Kang, N.; Ma, X.-L.; Cheng, H.-M.; Ren, W. Large-Area High-Quality 2D Ultrathin Mo₂C Superconducting Crystals. *Nat. Mater.* **2015**, *14*, 1135–1141.
- (22) Geng, D.; Zhao, X.; Chen, Z.; Sun, W.; Fu, W.; Chen, J.; Liu, W.; Zhou, W.; Loh, K. P. Direct Synthesis of Large-Area 2D Mo₂C on in Situ Grown Graphene. *Adv. Mater.* **2017**, *29*, 1700072.
- (23) Li, T.; Luo, W.; Kitadai, H.; Wang, X.; Ling, X. Probing the Domain Architecture in 2D α -Mo₂C via Polarized Raman Spectroscopy. *Adv. Mater.* **2019**, *31*, 1807160.
- (24) Xiao, X.; Yu, H.; Jin, H.; Wu, M.; Fang, Y.; Sun, J.; Hu, Z.; Li, T.; Wu, J.; Huang, L.; Gogotsi, Y.; Zhou, J. Salt-Templated Synthesis of 2D Metallic MoN and Other Nitrides. *ACS Nano* **2017**, *11*, 2180–2186.
- (25) Jauberteau, I.; Bessaudou, A.; Mayet, R.; Cornette, J.; Jauberteau, J.; Carles, P.; Merle-Méjean, T. Molybdenum Nitride Films: Crystal Structures, Synthesis, Mechanical, Electrical and Some Other Properties. *Coatings* **2015**, *5*, 656–687.
- (26) Ganin, A. Y.; Kienle, L.; Vajenine, G. V. Synthesis and Characterisation of Hexagonal Molybdenum Nitrides. *J. Solid State Chem.* **2006**, *179*, 2339–2348.
- (27) Bull, C. L.; Kawashima, T.; McMillan, P. F.; Machon, D.; Shebanova, O.; Daisenberger, D.; Soignard, E.; Takayama-Muromachi, E.; Chapon, L. C. Crystal Structure and High-Pressure Properties of γ -Mo₂N Determined by Neutron Powder Diffraction and X-Ray Diffraction. *J. Solid State Chem.* **2006**, *179*, 1762–1767.
- (28) Gray, M. J.; Kumar, N.; O'Connor, R.; Hoek, M.; Sheridan, E.; Doyle, M. C.; Romanelli, M. L.; Osterhoudt, G. B.; Wang, Y.; Plisson, V.; Lei, S.; Zhong, R.; Rachmilowitz, B.; Zhao, H.; Kitadai, H.; Shepard, S.; Schoop, L. M.; Gu, G. D.; Zeljkovic, I.; Ling, X.; Burch, K. S. A Cleanroom in a Glovebox. *Rev. Sci. Instrum.* **2020**, *91*, 073909.

- (29) Zhou, X.; Yan, M.; Dong, M.; Ma, D.; Yu, X.; Zhang, J.; Zhao, Y.; Wang, S. Phase Stability and Compressibility of 3R-MoN₂ at High Pressure. *Sci. Rep.* **2019**, *9*, 10524.
- (30) Splendiani, A.; Sun, L.; Zhang, Y.; Li, T.; Kim, J.; Chim, C.-Y.; Galli, G.; Wang, F. Emerging Photoluminescence in Monolayer MoS2. *Nano Lett.* **2010**, *10*, 1271–1275.
- (31) Lee, C.; Yan, H.; Brus, L. E.; Heinz, T. F.; Hone, J.; Ryu, S. Anomalous Lattice Vibrations of Single- and Few-Layer MoS₂. *ACS Nano* **2010**, *4*, 2695–2700.
- (32) Bae, S.; Kim, H.; Lee, Y.; Xu, X.; Park, J.-S.; Zheng, Y.; Balakrishnan, J.; Lei, T.; Kim, H. R.; Song, Y. I.; Kim, Y.-J.; Kim, K. S.; Özyilmaz, B.; Ahn, J.-H.; Hong, B. H.; Iijima, S. Roll-to-Roll Production of 30-Inch Graphene Films for Transparent Electrodes. *Nat. Nanotechnol.* **2010**, *5*, 574–578.
- (33) Ying, G.; Dillon, A. D.; Fafarman, A. T.; Barsoum, M. W. Transparent, Conductive Solution Processed Spincast 2D Ti₂CT_x (MXene) Films. *Mater. Res. Lett.* **2017**, *5*, 391–398.
- (34) Halim, J.; Lukatskaya, M. R.; Cook, K. M.; Lu, J.; Smith, C. R.; Näslund, L.-Å.; May, S. J.; Hultman, L.; Gogotsi, Y.; Eklund, P.; Barsoum, M. W. Transparent Conductive Two-Dimensional Titanium Carbide Epitaxial Thin Films. *Chem. Mater.* **2014**, *26*, 2374–2381.
- (35) Mariano, M.; Mashtalir, O.; Antonio, F. Q.; Ryu, W.-H.; Deng, B.; Xia, F.; Gogotsi, Y.; Taylor, A. D. Solution-Processed Titanium Carbide MXene Films Examined as Highly Transparent Conductors. *Nanoscale* **2016**, *8*, 16371–16378.
- (36) Acerce, M.; Voiry, D.; Chhowalla, M. Metallic 1T Phase MoS₂ Nanosheets as Supercapacitor Electrode Materials. *Nat. Nanotechnol.* **2015**, *10*, 313–318.
- (37) Huang, H.; Cui, Y.; Li, Q.; Dun, C.; Zhou, W.; Huang, W.; Chen, L.; Hewitt, C. A.; Carroll, D. L. Metallic 1T Phase MoS₂ Nanosheets for High-Performance Thermoelectric Energy Harvesting. *Nano Energy* **2016**, *26*, 172–179.
- (38) Urbankowski, P.; Anasori, B.; Hantanasirisakul, K.; Yang, L.; Zhang, L.; Haines, B.; May, S. J.; Billinge, S. J. L.; Gogotsi, Y. 2D Molybdenum and Vanadium Nitrides Synthesized by Ammoniation of 2D Transition Metal Carbides (MXenes). *Nanoscale* **2017**, *9*, 17722–17730.
- (39) Sun, Y.; Ding, S.; Xu, S.; Duan, J.; Chen, S. Metallic Two-Dimensional Metal-Organic Framework Arrays for Ultrafast Water Splitting. *J. Power Sources* **2021**, *494*, 229733.
- (40) Zhang, Z.; Niu, J.; Yang, P.; Gong, Y.; Ji, Q.; Shi, J.; Fang, Q.; Jiang, S.; Li, H.; Zhou, X.; Gu, L.; Wu, X.; Zhang, Y. Van Der Waals Epitaxial Growth of 2D Metallic Vanadium Diselenide Single Crystals and Their Extra-High Electrical Conductivity. *Adv. Mater.* **2017**, *29*, 1702359.
- (41) Zhao, S.; Hotta, T.; Koretsune, T.; Watanabe, K.; Taniguchi, T.; Sugawara, K.; Takahashi, T.; Shinohara, H.; Kitaura, R. Two-Dimensional Metallic NbS₂: Growth, Optical Identification and Transport Properties. 2D Mater. **2016**, *3*, 025027.
- (42) Kappera, R.; Voiry, D.; Yalcin, S. E.; Branch, B.; Gupta, G.; Mohite, A. D.; Chhowalla, M. Phase-Engineered Low-Resistance Contacts for Ultrathin MoS₂ Transistors. *Nat. Mater.* **2014**, *13*, 1128–1134.
- (43) Li, L.; Chen, J.; Wu, K.; Cao, C.; Shi, S.; Cui, J. The Stability of Metallic MoS₂ Nanosheets and Their Property Change by Annealing. *Nanomaterials* **2019**, *9*, 1366.
- (44) Habib, T.; Zhao, X.; Shah, S. A.; Chen, Y.; Sun, W.; An, H.; Lutkenhaus, J. L.; Radovic, M.; Green, M. J. Oxidation Stability of ${\rm Ti}_3{\rm C}_2{\rm T}_{\rm x}$ MXene Nanosheets in Solvents and Composite Films. *npj 2D Mater. Appl.* **2019**, *3*, 8.